Journal of Biomechanics 65 (2017) 216–220

Contents lists available at ScienceDirect

Journal of Biomechanics

journal homepage: www.elsevier.com/locate/jbiomech
www.JBiomech.com

Short communication

A strain-based finite element model for calcification progression in aortic valves

Amirhossein Arzani [a,*], Mohammad R.K. Mofrad [b]

[a] Mechanical Engineering Department, Northern Arizona University, Flagstaff, AZ, USA
[b] Bioengineering Department, University of California, Berkeley, CA, USA

ARTICLE INFO

Article history:
Accepted 15 October 2017

Keywords:
Calcific aortic valve disease
Finite element method
Transient structural mechanics
Mechanical strain

ABSTRACT

Calcific aortic valve disease (CAVD) is a serious disease affecting the aging population. A complex interaction between biochemicals, cells, and mechanical cues affects CAVD initiation and progression. In this study, motivated by the progression of calcification in regions of high strain, we developed a finite element method (FEM) based spatial calcification progression model. Several cardiac cycles of transient structural FEM simulations were simulated. After each simulation cycle, calcium deposition was placed in regions of high circumferential strain. Our results show the radial expansion of calcification as spokes starting from the attachment region, agreeing very well with the reported clinical data.

1. Introduction

Calcific aortic valve disease (CAVD) is the major form of aortic stenosis (Otto et al., 1997), where stiffening of the valve leaflets obstructs blood flow from the left ventricle into the systemic circulation. The initiation and progression of CAVD involve various interrelated mechanobiological processes spanning multiple scales (Pawade et al., 2015). Hemodynamics phenomena play an important role in normal aortic valve function and CAVD (Sacks and Yoganathan, 2007; Balachandran et al., 2011; Gould et al., 2013; Ayoub et al., 2016). Wall shear stress exerted on the valvular endothelial cells (ECs) influences the inflammatory processes in CAVD as well as the signaling between the ECs and the valvular interstitial cells (VICs). Mechanical strains sensed by the VICs are believed to promote VIC differentiation to a calcific phenotype (Fisher et al., 2013).

Calcification is more likely to occur on the aortic side of the valve (Otto et al., 1994; Weinberg et al., 2010; Yip and Simmons, 2011), which has been attributed to the disturbed hemodynamics (Weinberg et al., 2010; Ge and Sotiropoulos, 2010) and the structural distinctions (Neufeld et al., 2014). Although progress has been made in modeling the aortic valve biomechanics, modeling CAVD progression has not received much attention. Previous biomechanical aortic valve calcification progression models have either obtained calcification progression from medical imaging data (Halevi et al., 2015), used pre-assumed simple growth laws (Weinberg et al., 2009), or have not reported the calcification growth patterns (Katayama et al., 2013).

Herein, we propose a calcification model based on the observation that mechanical strain promotes calcification in aortic valves (Balachandran et al., 2010; Hutcheson et al., 2012; Fisher et al., 2013; Hsu et al., 2016). We propose an algorithm to model the long-term evolution of calcification based on the mechanical strain on the aortic side of the valve. CAVD initiation and progression involve a complex interplay between various biochemicals, cells, and biomechanical factors (Arzani et al., 2017). In the current study, motivated by the known self-perpetuating process of calcification (Pawade et al., 2015), we simulate the spatial calcification growth patterns based on the mechanical strain obtained from a finite element model.

2. Methods

2.1. Finite element method (FEM)

The idealized aortic valve geometrical model used in prior studies (Weinberg and Mofrad, 2007; Weinberg et al., 2009) was used in this study. The model included the valve leaflet with varying thickness, the aortic root and sinus, and the ascending aorta (Fig. 1). We assumed perfect symmetry of the valve to reduce the computational domain to one-sixth of the valve, similar to previous studies (Weinberg and Mofrad, 2007; Weinberg et al., 2009; Joda et al., 2016). This is a favorable assumption because several cycles of simulation need to be performed. The model was discretized into 192k second order tetrahedral elements with higher

* Corresponding author.
E-mail address: amir.arzani@nau.edu (A. Arzani).

https://doi.org/10.1016/j.jbiomech.2017.10.014
0021-9290/

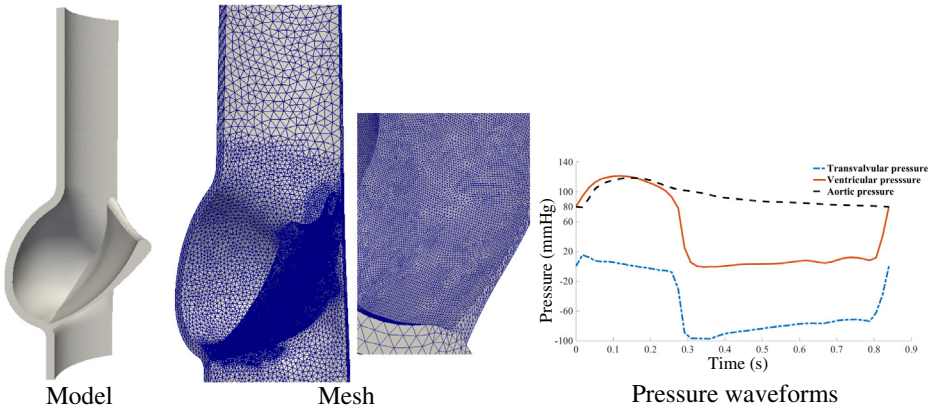

Fig. 1. The computational domain and mesh used in the finite element calculations. The pressure waveforms shown were obtained from Levick (2010) and used as the boundary conditions.

resolution in the leaflet and attachment region (Fig. 1). The mesh was constructed using SimVascular (Updegrove et al., 2017). A mesh independence study using third order elements was performed to verify the results.

A single term Mooney-Rivlin constitutive law, $W_{wall} = c_{wall}(I_1 - 3)$, was assumed for the aortic wall (Weinberg and Mofrad, 2007). The aortic valve was assumed transversely isotropic with the collagen fibers aligned in the circumferential direction using the constitutive law proposed by Humphrey and Yin (1987):

$$W = c\{\exp[c_1(I_1 - 3)] - 1\} + c_0\left\{\exp\left[c_2(\sqrt{I_4} - 1)^2\right] - 1\right\} + \frac{1}{2}\kappa(J-1)^2, \quad (1)$$

where I_1 is the first invariant of the right Cauchy-Green strain tensor ($\mathbf{C}$), J is the Jacobian determinant or volume ratio, $I_4 = \mathbf{C} : \mathbf{a_0} \otimes \mathbf{a_0}$ is the square of the fiber stretch along the circumferential direction ($\mathbf{a_0}$), and κ is a sufficiently large parameter used to impose a nearly incompressible material behavior. The anisotropic term (second term) is only switched on if $I_4 \geqslant 1$. The constant c_{wall} was set to 0.33 MPa. At low strains, this choice recovers the constant material stiffness of 2 MPa used in prior studies (Conti et al., 2010; Sturla et al., 2016; Cao and Sucosky, 2017). The constants in Eq. (1) were fitted to the experimental data of valve leaflets and reported in a prior study (Auricchio et al., 2012). These material constants are given in Table 1. A density of 1100 kg/m^3 was used for the tissues (Conti et al., 2010). The pressure waveforms shown in Fig. 1 obtained from Levick (2010) were applied as boundary conditions. Namely, the transient aortic and ventricular pressure waveforms were applied to the inner aortic wall above and below the valve leaflet, and the transvalvular pressure waveform was applied to the aortic or ventricular side of the valve leaflet, depending on the pressure sign. Only radial expansion was allowed at the ends of the aortic wall. A symmetry boundary condition was applied weakly at the plane of symmetry using the Nitsche method (Freund and Stenberg, 1995; Stenberg, 1995) with a sufficiently large penalty-like parameter. The Cauchy's equation of motion was formulated in the reference configuration (Ogden, 1997) for a nearly incompressible material (Holzapfel et al., 2000) and solved using a second order finite element method implemented in FEniCS (Logg et al., 2012). Time integration was performed using the generalized-α method (Chung and Hulbert, 1993) with sufficiently small time steps to ensure the convergence of the nonlinear Newton solver.

Table 1
The parameters used in the constitutive model (obtained from Auricchio et al. (2012)).

c	c_1	c_0	c_2
0.022 MPa	5.81	0.062 MPa	24.97

2.2. Calcification algorithm

Here we describe the proposed solely strain-based calcification algorithm. Calcification was only allowed for the elements on the aortic side of the valve. A cardiac cycle of simulation was performed to obtain the peak temporal circumferential strain for each element on the aortic side of the valve. To emphasize that our model does not capture the temporal evolution, we will refer to each cardiac cycle as a simulation cycle. The computed strain was projected to the element because in our model calcification occurs element-wise. If the calculated strain was larger than a certain threshold the element calcified. Calcification was modeled by increasing the stiffness of the element. This was done by increasing the material constant (c) in the isotropic term of the constitutive model (first term in Eq. (1)) proportional to the strain and a stiffening factor (see Algorithm 1). We have assumed that calcium deposition does not affect the anisotropic behavior of the leaflet, which is due to the collagen fibers. The simulation cycle was repeated after calcification to obtain the updated peak temporal circumferential strains. This procedure was repeated until no more calcification could happen. That is, either there were no more elements with strains higher than the threshold or the calcifying elements (elements with high strain) had reached a predefined peak stiffness.

The strain threshold for calcification was chosen as 0.05 based on in vitro data (Fisher et al., 2013). Note that a peak strain of 0.05 is within the physiological range of strain, however, under pathological conditions certain biochemicals such as transforming growth factor-β promote myofibroblastic or osteogenic differentiation of VICs, and therefore calcification. Our calcification model is intended to represent such conditions. The maximum stiffness that a calcified element can reach (*MAT_const_max*) is defined to be orders of magnitude larger than the material constant (Wong et al., 2012; Holzapfel et al., 2002; Halevi et al., 2015). In the algorithm, if the updated material constant exceeded this maximum value, the maximum value was used as the new material constant. Algorithm 1 illustrates the details of the calcification algorithm, and Table 2 gives the parameters used in the algorithm.

Algorithm 1. The strain-based calcification algorithm.

Define ϵ_{thr}, *MAT_const_max*, Stiffen_factor
while $\epsilon_{max} \geqslant \epsilon_{thr}$ and *Mat_const* $<$ *MAT_const_max* **do**
  for $t = 0$ to T (cardiac cycle) **do**
    Find temporal ϵ_{max} locally
  end for
  if $\epsilon_{max} \geqslant \epsilon_{thr}$ **then**
    $Mat\_const \leftarrow Mat\_const \times Stiffen\_factor \times \frac{\epsilon_{max}}{\epsilon_{thr}}$
    if *Mat_const* $>$ *MAT_const_max* **then**
      $Mat\_const \leftarrow MAT\_const\_max$
    end if
  end if
end while

Table 2
The parameters used in the calcification algorithm.

ϵ_{thr}	*MAT_const_max*	*Stiffen_factor*
0.05	$c * 1000$ (MPa)	100

3. Results

The calcification algorithm was repeated until the stop criteria were reached after the 19th simulation cycle. The calcification progression results are shown in Fig. 2. The color bar represents the material constant (c) in the isotropic term of the constitutive equation, and therefore, an indicator of calcification intensity. The six snapshots (Fig. 2(a)–(f)) show the calcification progression at different steps. The first and last snapshots represent the first and last simulation cycles. It is observed that calcification starts at the base of the valve leaflet and expands towards the center of the leaflet. This radial expansion mostly happens as different spokes extending towards the center of the leaflet. Interestingly, this is similar to the calcification growth pattern observed by Thubrikar et al. (1986), which is shown in Fig. 2(g).

The variations in the circumferential strain during calcification progression are shown in Fig. 3. The maximum diastolic circumferential strain without calcification was 0.1, agreeing with the data reported in the literature (Thubrikar, 1989; Lo and Vesely, 1995; Balachandran et al., 2011). The snapshots correspond to those shown in Fig. 2. Each snapshot shows the peak circumferential strain on the aortic side of the valve during the simulation cycle in which the corresponding calcium deposition occurs. The strain distribution is visualized in an element-wise fashion, and therefore creating the non-smooth patterns observed in the figure. It is observed that a band of high strain initiates at the attachment region and propagates towards the center of the leaflet.

A schematic of the strain-driven calcification growth pattern is illustrated in Fig. 4. Initially, a band of high strain is formed at the

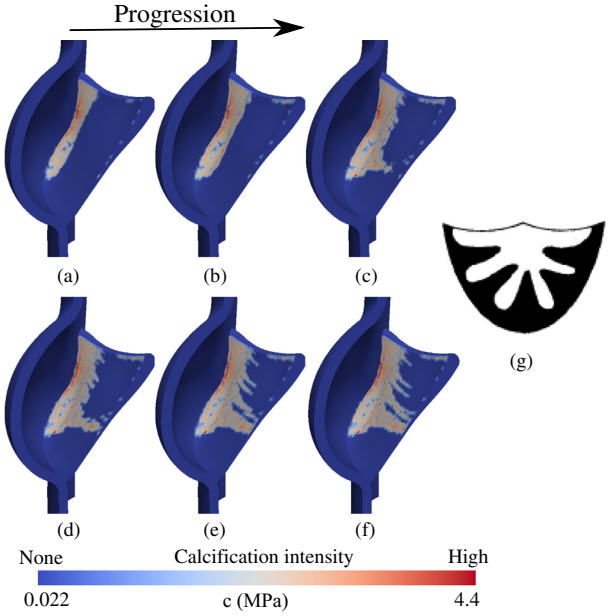

Fig. 2. Calcification growth at different snapshots (a)–(f). The color bar represents the isotropic material constant c in Eq. (1) and the calcification intensity. (g) One of the two calcification growth patterns observed in most of the patients studied by Thubrikar et al. (1986). Figure reproduced with permission from Thubrikar et al. (1986). Copyright 1986 Elsevier. (For interpretation of the references to color in this figure legend, the reader is referred to the web version of this article.)

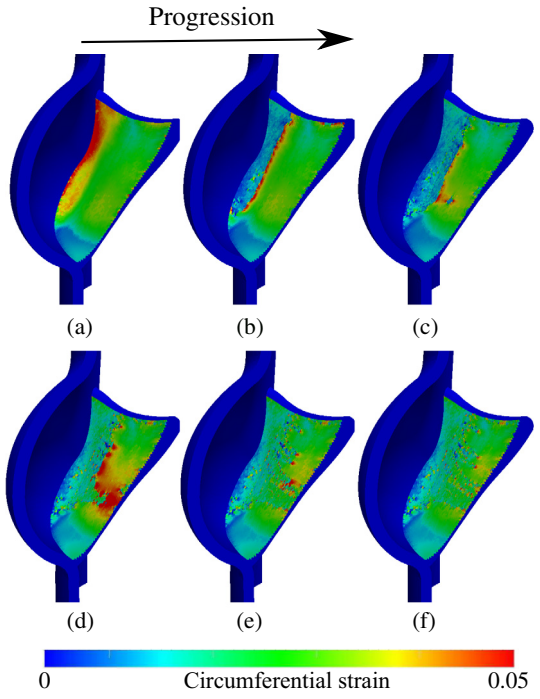

Fig. 3. Temporal peak circumferential strain at different snapshots (a)–(f). The snapshots correspond to those shown in Fig. 2. That is, the peak strain shown here is used for the corresponding calcium deposition shown in Fig. 2. Results are only shown on the aortic side of the valve. An element-wise visualization is used, consistent with the numerical calcification algorithm.

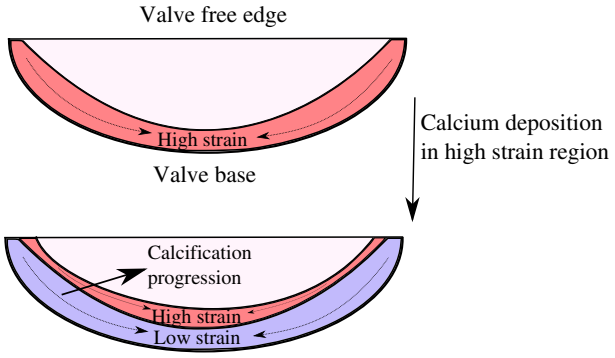

Fig. 4. The proposed strain-based aortic valve calcification growth pattern. Calcification starts at the attachment where high mechanical strain exists and propagates radially towards the center of the leaflet. Calcium deposition reduces the strain in its region of influence; however, the created compliance mismatch leads to an increase in strain at the border of the calcification region.

base of the valve. Upon calcification in this region, a compliance mismatch is created at the boundary of the calcified and noncalcified regions. This compliance mismatch leads to a localized increase in strain, which leads to further calcium deposition and the propagation of calcification. Calcium deposition increases the valve stiffness, and therefore reducing strain in the calcified region. This reduction in strain is not uniform, because of the spatially non-uniform calcification, which is proportional to the strain.

4. Discussion

We presented a new strain-based FEM model for simulation of the long-term spatial progression of calcification in the aortic valve. Our model is able to replicate the clinically observed radial calcification expansion patterns (Thubrikar et al., 1986). Calcification creates a localized increase in stiffness, resulting in a compliance mismatch at the boundary of calcification that ultimately drives the observed spatial growth patterns. Interestingly, more recent studies have also shown the radial expansion of calcification in CAVD (Sturla et al., 2016). Our results support the hypothesis that once calcification is established, further calcium deposition is driven mainly by calcium itself (Pawade et al., 2015). It should be pointed that our model does not consider the biochemical factors that play an important role in early stages of CAVD. We are assuming that these biochemicals are present at a sufficient amount (a pathological scenario) and calcification initiation and progression happen in regions of high strain.

Our model does not quantify the temporal progression of CAVD. We have previously developed a systems biology model for capturing the temporal evolution of CAVD (Arzani et al., 2017). In our current model, calcification is driven by a stiffening factor applied to the regions of high circumferential strain. The stiffening factor had to be large enough to initiate a notable compliance mismatch for calcification progression. In reality, stiffening happens with a certain time scale. However, since we are not modeling the temporal dynamics of calcification, the precise magnitude of this parameter is not important. Our results showed that as calcification progressed further, a decreased area of the valve would be exposed to the required compliance mismatch to drive further calcification, thereby reducing the rate of spatial calcification progression. Interestingly, this is similar to the observed biphasic clinical risk of coronary artery calcification (Hsu et al., 2016).

In order to apply our calcification model to clinical diagnosis, our model needs to become patient-specific. Medical imaging data could be used to construct an image-based model of the aortic root and valve. However, obtaining patient-specific constitutive material properties is not clinically feasible. The strain threshold for calcification depends on the biochemical environment among other potential factors. The coupling of our model with systems biology models could be an alternative to account for the biochemical environment (Arzani et al., 2017). We investigated the effect of the strain threshold (0.05) in our model. Minimal calcification progression was observed if the strain threshold was increased close to the spatiotemporal peak strain of 0.1.

Our study has some limitations. Fluid structure interaction (FSI) modeling could be used to increase the accuracy of the valve dynamics and strain distribution. We ignored the fluid dynamics and relied on a structural mechanics finite element model in our study. This helps to run several simulation cycles (19 in this study) more efficiently by significantly reducing the computational cost. Moreover, it has been shown that the strains computed with FSI are not significantly different than structural FEM (Sturla et al., 2013). We have assumed that calcification only happens at the computational elements on the aortic side of the valve, and we have ignored changes in thickness due to calcification. Our model assumed perfect symmetry to reduce the computational domain. This is anticipated to have minimal effect on our model as we have assumed an idealized model with symmetric geometry. Our calcification model assumes a pathological scenario where calcification is initiated in regions of high strain. We have ignored the biochemical processes that contribute to the initiation and progression of calcification. In our model, calcification is initiated in regions of high strain and further calcification progression is driven by the strain concentration resulting from the compliance mismatch. Indeed, localized increase in strain has been reported for calcified valves (Halevi et al., 2015).

In conclusion, we have developed a solely strain-driven model that closely captures the experimentally observed CAVD spatial progression patterns. Our results show radial expansion of calcification starting from the base of the valve leaflet, in close agreement with the aortic valve calcification distinct geometrical features reported in the literature (Thubrikar et al., 1986; Sturla et al., 2016).

Conflicts of interest

None.

Acknowledgements

This work was supported by the American Heart Association (Award 16GRNT27630015).

References

Arzani, A., Masters, K.S., Mofrad, M.R.K., 2017. Multiscale systems biology model of calcific aortic valve disease progression. ACS Biomater. Sci. Eng. <https://doi.org/10.1021/acsbiomaterials.7b00174>.

Auricchio, F., Ferrara, A., Morganti, S., 2012. Comparison and critical analysis of invariant-based models with respect to their ability in fitting human aortic valve data. Ann. Solid Struct. Mech. 4 (1–2), 1–14.

Ayoub, S., Ferrari, G., Gorman, R.C., Gorman, J.H., Schoen, F.J., Sacks, M.S., 2016. Heart valve biomechanics and underlying mechanobiology. Comprehen. Physiol. <https://doi.org/10.1002/cphy.c150048>.

Balachandran, K., Sucosky, P., Jo, H., Yoganathan, A.P., 2010. Elevated cyclic stretch induces aortic valve calcification in a bone morphogenic protein-dependent manner. Am. J. Pathol. 177 (1), 49–57.

Balachandran, K., Sucosky, P., Yoganathan, A.P., 2011. Hemodynamics and mechanobiology of aortic valve inflammation and calcification. Int. J. Inflamm. 2011, 1–15. https://doi.org/10.4061/2011/263870.

Cao, K., Sucosky, P., 2017. Computational comparison of regional stress and deformation characteristics in tricuspid and bicuspid aortic valve leaflets. Int. J. Numer. Methods Biomed. Eng., 1–21 https://doi.org/10.1002/cnm.2798.

Chung, J., Hulbert, G.M., 1993. A time integration algorithm for structural dynamics with improved numerical dissipation: the generalized-α method. J. Appl. Mech. 60 (2), 371–375.

Conti, C.A., Votta, E., Della Corte, A., Del Viscovo, L., Bancone, C., Cotrufo, M., Redaelli, A., 2010. Dynamic finite element analysis of the aortic root from MRI-derived parameters. Med. Eng. Phys. 32 (2), 212–221.

Fisher, C.I., Chen, J., Merryman, W.D., 2013. Calcific nodule morphogenesis by heart valve interstitial cells is strain dependent. Biomech. Model. Mechanobiol. 12 (1), 5–17.

Freund, J., Stenberg, R., 1995. On weakly imposed boundary conditions for second order problems. In: Proceedings of the Ninth Int. Conf. Finite Elements in Fluids, pp. 327–336.

Ge, L., Sotiropoulos, F., 2010. Direction and magnitude of blood flow shear stresses on the leaflets of aortic valves: is there a link with valve calcification? J. Biomech. Eng. 132 (1), 014505.

Gould, S.T., Srigunapalan, S., Simmons, C.A., Anseth, K.S., 2013. Hemodynamic and cellular response feedback in calcific aortic valve disease. Circul. Res. 113 (2), 186–197.

Halevi, R., Hamdan, A., Marom, G., Mega, M., Raanani, E., Haj-Ali, R., 2015. Progressive aortic valve calcification: three-dimensional visualization and biomechanical analysis. J. Biomech. 48 (3), 489–497.

Holzapfel, G.A., Gasser, T.C., Ogden, R.W., 2000. A new constitutive framework for arterial wall mechanics and a comparative study of material models. J. Elast. Phys. Sci. Solids 61 (1–3), 1–48.

Holzapfel, G.A., Stadler, M., Schulze-Bauer, C.A.J., 2002. A layer-specific three-dimensional model for the simulation of balloon angioplasty using magnetic resonance imaging and mechanical testing. Ann. Biomed. Eng. 30 (6), 753–767.

Hsu, J.J., Lim, J., Tintut, Y., Demer, L.L., 2016. Cell-matrix mechanics and pattern formation in inflammatory cardiovascular calcification. Heart, heartjnl–2016.

Humphrey, J.D., Yin, F.C.P., 1987. On constitutive relations and finite deformations of passive cardiac tissue: I. A pseudostrain-energy function. J. Biomech. Eng. 109 (4), 298–304.
Hutcheson, J.D., Venkataraman, R., Baudenbacher, F.J., Merryman, W.D., 2012. Intracellular Ca 2+ accumulation is strain-dependent and correlates with apoptosis in aortic valve fibroblasts. J. Biomech. 45 (5), 888–894.
Joda, A., Jin, Z., Haverich, A., Summers, J., Korossis, S., 2016. Multiphysics simulation of the effect of leaflet thickness inhomogeneity and material anisotropy on the stress–strain distribution on the aortic valve. J. Biomech. 49 (12), 2502–2512.
Katayama, S., Umetani, N., Hisada, T., Sugiura, S., 2013. Bicuspid aortic valves undergo excessive strain during opening: a simulation study. J. Thoracic Cardiovascul. Surg. 145 (6), 1570–1576.
Levick, J.R., 2010. An Introduction to Cardiovascular Physiology. Hodder Arnold, London.
Lo, D., Vesely, I., 1995. Biaxial strain analysis of the porcine aortic valve. Ann. Thoracic Surg. 60, S374–S378.
Logg, A., Mardal, K.A., Wells, G., 2012. Automated Solution of Differential Equations by the Finite Element Method, vol. 84. Springer, Berlin, Heidelberg.
Neufeld, E.B., Zadrozny, L.M., Phillips, D., Aponte, A., Yu, Z.X., Balaban, R.S., 2014. Decorin and biglycan retain LDL in disease-prone valvular and aortic subendothelial intimal matrix. Atherosclerosis 233 (1), 113–121.
Ogden, O.W., 1997. Non-linear Elastic Deformations. Courier Corporation.
Otto, C.M., Burwash, I.G., Legget, M.E., Munt, B.I., Fujioka, M., Healy, N.L., Kraft, C.D., Miyake-Hull, C.Y., Schwaegler, R.G., 1997. Prospective study of asymptomatic valvular aortic stenosis clinical, echocardiographic, and exercise predictors of outcome. Circulation 95 (9), 2262–2270.
Otto, C.M., Kuusisto, J., Reichenbach, D.D., Gown, A.M., O'Brien, K.D., 1994. Characterization of the early lesion of 'degenerative' valvular aortic stenosis. Histological and immunohistochemical studies. Circulation 90 (2), 844–853.
Pawade, T.A., Newby, D.E., Dweck, M.R., 2015. Calcification in aortic stenosis: the skeleton key. J. Am. College Cardiol. 66 (5), 561–577.
Sacks, M.S., Yoganathan, A.P., 2007. Heart valve function: a biomechanical perspective. Philosoph. Trans. Roy. Soc. Lond. B: Biol. Sci. 362 (1484), 1369–1391.
Stenberg, R., 1995. On some techniques for approximating boundary conditions in the finite element method. J. Comput. Appl. Math. 63 (1–3), 139–148.
Sturla, F., Ronzoni, M., Vitali, M., Dimasi, A., Vismara, R., Preston-Maher, G., Burriesci, G., Votta, E., Redaelli, A., 2016. Impact of different aortic valve calcification patterns on the outcome of transcatheter aortic valve implantation: a finite element study. J. Biomech. 49 (12), 2520–2530.
Sturla, F., Votta, E., Stevanella, M., Conti, C.A., Redaelli, A., 2013. Impact of modeling fluid–structure interaction in the computational analysis of aortic root biomechanics. Med. Eng. Phys. 35 (12), 1721–1730.
Thubrikar, M.J., 1989. The Aortic Valve. CRC Press.
Thubrikar, M.J., Aouad, J., Nolan, S.P., 1986. Patterns of calcific deposits in operatively excised stenotic or purely regurgitant aortic valves and their relation to mechanical stress. Am. J. Cardiol. 58 (3), 304–308.
Updegrove, A., Wilson, N.M., Merkow, J., Lan, H., Marsden, A.L., Shadden, S.C., 2017. Simvascular: an open source pipeline for cardiovascular simulation. Ann. Biomed. Eng. 45 (3), 525–541.
Weinberg, E.J., Mack, P.J., Schoen, F.J., García-Cardeña, G., Mofrad, M.R.K., 2010. Hemodynamic environments from opposing sides of human aortic valve leaflets evoke distinct endothelial phenotypes in vitro. Cardiovascul. Eng. 10 (1), 5–11.
Weinberg, E.J., Mofrad, M.R.K., 2007. Transient, three-dimensional, multiscale simulations of the human aortic valve. Cardiovascul. Eng. 7 (4), 140–155.
Weinberg, E.J., Schoen, F.J., Mofrad, M.R.K., 2009. A computational model of aging and calcification in the aortic heart valve. PLoS One 4 (6), e5960.
Wong, K.K.L., Thavornpattanapong, P., Cheung, S.C.P., Sun, Z., Tu, J., 2012. Effect of calcification on the mechanical stability of plaque based on a three-dimensional carotid bifurcation model. BMC Cardiovascul. Disorders 12 (1), 7.
Yip, C.Y.Y., Simmons, C.A., 2011. The aortic valve microenvironment and its role in calcific aortic valve disease. Cardiovascul. Pathol. 20 (3), 177–182.